Solid Earth Discuss., 7, 1059–1076, 2015
www.solid-earth-discuss.net/7/1059/2015/
doi:10.5194/sed-7-1059-2015

Solid Earth Discussions
Open Access

Quantizing Earth surface deformations

C. O. Bowin[1], W. Yi[2], R. D. Rosson[3], T. S. Bolmer[1], and W. J. Sass[1]

[1]Wood Hole Oceanographic Institution, Woods Hole, MA, USA
[2]Intelligent Solutions Group, John Deere, Kaiserslautern, Germany
[3]Applications Engineering Group, MathWorks, Natick, MA, USA

Received: 29 December 2014 – Accepted: 14 January 2015 – Published: 9 March 2015

Correspondence to: C. O. Bowin (cbowin@whoi.edu)

Published by Copernicus Publications on behalf of the European Geosciences Union.

Abstract

The global analysis of Bowin (2010) used the global 14 absolute Euler pole set (62 Myr history) from Gripp and Gordon (1990) and demonstrated that plate tectonics conserves angular momentum. We herein extend that analysis using the more detailed Bird (2003) 52 present-day Euler pole set (relative to a fixed Pacific plate) for the Earth's surface, after conversion to absolute Euler poles. Additionally, new analytical results now provide new details on upper mantle mass anomalies in the outer 200 km of the Earth, as well as an initial quantizing of surface deformations.

1 Introduction

Several developments have recently coalesced, and now provide us with the ability not only to understand the how and why the Earth surface deforms (see Fig. 1), but also to make a preliminary numerical magnitude classification of Earth surface deformations. The first development step was adopting the use of ratios of gravity over geoid (g/N) values at anomaly centers to estimate an equivalent point-mass depth and mass of the causative mass anomalies (Bowin, 2000). The Earth's power spectrum has a sharp reduction in slope after degree 3. So, whether we look at the geoid degree 2–10, degree 2–100, 2–250 (GEM-t2), NGM2008, GRACE, or GOCE fields, are all dominated by the 2–3 coefficient values. For the mass distribution inthe Earth, the g/N (mgal m^{-1}) ratio for the core-mantle boundary (CMB) lies just above the point mass depth for harmonic degree 3 (Bowin, 2000, Fig. 8). Thus, that break in slope in the Earth's potential power spectrum curve closely coincides with the change from a deep dense metallic core to an upper silicate mantle.

The second development was the discovery of the hidden positive mass anomaly pattern buried amongst the spherical harmonic degree 4–10 coefficients that coincide with the locations of present day plate subduction zones. See, for example (Bowin, 2000, Figs. 6 and 4–10).

SED
7, 1059–1076, 2015

A third development was then the new finding that the tectonic plates of the Earth very slowly accelerate and decelerate at rates that are about 10^{-8} times smaller than plate velocities (Bowin and Kuiper, 2005; Bowin, 2009, 2010), whereas previously the consensus had been that there appeared to have been no net torque amongst the fourteen, or so, principal Earth plates (e.g. Gripp and Gordon, 2002). That Gripp and Gordon paper also cataloged the absolute motion Euler pole locations of each plate at 2 my intervals over the past 62 myrs. Using those results Bowin (2010) was then able to demonstrated that if a plate were to slow down, then other plates would have to speed up, so that globally, plate tectonics conserves angular momentum ($\sim 1.4 \times 10^{27}\,\mathrm{kg\,m^2\,s^{-1}}$). This angular momentum for the Earth's plate tectonic system is much smaller than that of the Earth/moon system ($2.88 \times 10^{34}\,\mathrm{kg\,m^2\,s^{-1}}$), and, is in turn, comparable to the much greater angular momentum of our solar system ($8.95 \times 10^{43}\,\mathrm{kg\,m^2\,s^{-1}}$).

The fourth development was the unexpected finding that the absolute motions along the common boundary of the Pacific and Australian plates, the past 40 plus million years, have been at nearly 90° to each other. Thus it is difficult to form a mental image of how the Indonesian island subduction zone along the northern edge of the Australian plate is interacting at depth with a westward moving Pacific plate, particularly, if one wants both plates to be simple "roller" type cells. The strong limitation that this observation places on mantle convection, leads us to view present mantle dynamics as resulting from the sinking of the dense "phase-change" minerals in the subducted lithosphere, which serves angular momentum and perpetuates plate motions.

Lastly, since we now understand deformation to result from an impulse (a change of momentum) in plate tectonic motions, we sought some means by which we might try to quantify such deformations. Our initial experiments given here utilize the local maximum topography gradient as a deformation index value.

SED
7, 1059–1076, 2015

2 Deriving high derivative earth potential field model

The gravity field coefficients are estimated with high accuracy in the long wavelength part (corresponding to the coefficients of low degrees). Our derived filtered spherical harmonic coefficients for degrees 2–264 are given in the accompanied Supplement.

Various alternative methods exist for the determination of global gravity field models, such as integration on Earth sphere, least square adjustment or collocation, and various data sources are used, such as satellite based data or terrestrial (surface) observations. The error behaviors of the resulting gravity field models depend on the method, the quality and properties of the observations. In general, the gravity field is not homogeneously determined. With satellite gravimetry the high frequency part (corresponding to the gravity field coefficients of higher degrees) is computed less accurate as the low frequency part. This results some short wavelength noise in the computed gravity field models. It is therefore necessary to filter the signal and thereby suppress the noise.

The idea of filtering gravity field models in the spectral domain is based on smooth SH coefficients with some depression factors. There are various smooth functions based on such as (Pellinen, 1966) and (Jekeli, 1981), etc. With Gaussian mean filter in the spectral domain as an example, as presented by Jekeli (1981), the recursive formula for a Gaussian smoothing coefficients in the spectral domain is given as

$$\beta_0 = 1$$

$$\beta_1 = \frac{1 + e^{-2b}}{1 - e^{-2b}} - \frac{1}{b}$$

$$\beta_n = \frac{-2n + 3}{b}\beta_{n-1} + \beta_{n-2}, \quad n \geq 3$$

Where $b = \frac{\ln 2}{1-\cos(r/R_\oplus)}$ with r the radius of a spherical cap to be smoothed and $R_\oplus$ the radius of the Earth.

SED
7, 1059–1076, 2015

Using the above filter coefficients, the filtered gravity field coefficients can be derived as

$$\begin{Bmatrix} \overline{C'}_{nm} \\ \overline{S'}_{nm} \end{Bmatrix} = \beta_n \begin{Bmatrix} \overline{C}_{nm} \\ \overline{S}_{nm} \end{Bmatrix}$$

The gravity field coefficients are estimated with high accuracy in the long wavelength part (corresponding to the coefficients of low degrees). In order to avoid filtering these low degree coefficients, we shift the damping factors above to a certain degree n_0, and obtain a new set of filter coefficients such that

$$\beta'_n = 1, \quad n < n_0$$

$$\beta'_n = \beta_{n-n_0}, \quad n \geq n_0$$

The gravity field coefficients are estimated with high accuracy in the long wavelength part (corresponding to the coefficients of low degrees). In order to avoid filtering these low degree coefficients, we shift the damping factors above to a certain degree (30), and obtain a new set of filter coefficients such that have yielded stable estimates of global geoid, gravity, vertical gravity gradient, and vertical gradient of vertical gravity gradient anomaly values for degrees 31–264. These coefficients reflect mass anomalies that exist in the outer 200 km of the Earth.

Plots of our results are shown in Fig. 2 for degree 31–264 contributions for geoid, gravity, vertical gravity gradient, and vertical gradient of vertical gravity gradient together all demonstrate that the only principal mass anomalies in the outer 200 km of the Earth are those of the negative mass anomalies associated with fore-arc lithosphere depressions, and the positive mass anomalies of the uplifted island arc/mountain ranges.

SED
7, 1059–1076, 2015

3 Motions of the Earth's tectonic plates and earthquakes

Bowin (2010) demonstrated that plate tectonics conserves angular momentum using the 14 major tectonic plate history of the Earth (except the Juan de Fuca and Philippine plates). Euler stage pole histories the past 62 million years of Gripp and Gordon (1990) were given. We believe it bears restating the mirroring of the bend in the Emperor–Hawaiian seamount chain in the locations of the 4448 filtered stage pole locations for the absolute motions of the Nazca plate (Bowin, 2010, Plate No. 11, Fig. 12) gives credence to both the quaternion analysis utilized and the role of impulse in plate motions. Of the 14 plates analyzed, the Nazca plate is the only one that has a stage pole pattern revealing such a pronounced bend in stage pole trend at 46 Myr.

For this present study of active surface deformation we have chosen to use a more detailed 52 tectonic plate model of the Earth's surface by Bird (2003). Bird's published Euler pole values are relative to a fixed Pacific plate. An important contribution was provided by Rick Rosson (PC, 2011) of Mathworks, who converted Bird's 52 relative Euler poles to absolute poles of rotation (Table 1).

Although the rates of plate acceleration/deceleration are very small, they are real, and thus indicate that impulse (force multiplied by time) due to changes in plate momentums (plate mass multiplied by velocity) are what cause deformations within the Earth and on its surface. Thus one of our early tasks was to display the individual plate motion vectors for the 52 plates utilizing the absolute rotation Euler pole data of Table 1 on a global rectangular grid having a 5 arcmin spacing (see Fig. 1, and top pdf file in the Supplement).

Earthquakes result from the release of strain that accumulates in the Earth, and those strains, in turn, result from plate motions. Therefore, this dependency proves that the maximum energy for seismicity is similarly bounded. Thus, we contend that this new knowledge of plate acceleration/deceleration opens a new portal through which earthquakes and lithospheric strain accumulation must now be viewed. We can now state that there will NEVER be a magnitude 12 earthquake. We can also confidently

SED
7, 1059–1076, 2015

state that there will NEVER be a magnitude 11 earthquake. We cannot rule out the possibility that earthquakes of a very low magnitude 10 might occur. This is because the time constant for strain build up in the crust is on the order of thousands of years, and we only have barely a century of observations. Furthermore, at the present GPS receiver sensitivities, nearly 100 years of observations are required to directly assess present day plate accelerations.

4 What is going on inside the Earth?

Bowin (2010) demonstrated that it is the sinking of the positive phase change mass anomalies of the subducted lithosphere that drives plate tectonics. The present locations of those positive mass anomalies are most clearly revealed in the spherical harmonic degree 4–10 coefficient packet of the Earth's potential field. As the linear bands of subducted lithosphere gradually shift locations so, too, will the 4–10 coefficients change. The mass anomalies represented by the degree 2–3 coefficients are about an order of magnitude greater (10^{23} g) than those of the degree 4–10 packet (10^{22} g) (Bowin, 2000, Fig. 7), and are considered to reflect lateral mass variations due to topography of the core/mantle boundary (CMB).

Since the Earth's rotation rate is gradually slowing down due to tidal perturbations from the Earth's moon, and in a year's time, presently, the moon's center of mass moves about 2 cm further away from the Earth's center of mass. Thereby conserving angular momentum of the Earth/moon system ($2.88 \times 10^{34}\,\mathrm{kg\,m^2\,s^{-1}}$). And, this is, in turn, similar to the much greater conservation of angular momentum of our solar system ($8.95 \times 10^{43}\,\mathrm{kg\,m^2\,s^{-1}}$). But interestingly, we've now learned that our solar system is odd. Our central sun has a mass equal to 99 % of the total solar system's mass, yet the sun has only ~ 4 % of its angular momentum. The most common interpretation has been the nebular hypothesis in which the mass of the sun has remained nearly constant, but it does not explain the solar system's angular momentum puzzle. However, we favor the new interpretation of James Constant of a closed solar

SED
7, 1059–1076, 2015

system in which during its earliest epochs, the sun should have been spinning slower with less mass at longer radius, and the planets should have been orbiting faster with more mass at shorter radii (Constant, 2015).

The fact that hot lava erupts from volcanoes that build up upon the Earth's surface helps to document that the Earth's interior is warmer than it's surface, as does the common increase in temperature with depth in drill holes. It is easy to see how the image of a hot Earth interior, combined with a view of a convecting pot of chicken noodle soup could inspire the notion of a thermal convecting mantle as a driver for plate tectonics. So the concept of a thermally convecting mantle has come to dominate the geophysical community's interpretation of the driving mechanism of plate tectonics.

However, a reexamination of Fig. 1 now necessitates revising that opinion of a thermally convecting mantle. In particular, note that the absolute easterly motion of the direction of the Pacific (PA) plate, from the north end of the Tonga trench to the south end of the Yap trench, is essentially at 90° to the northerly motion of the Australian (Au) adjacent plate to the south. Efforts to visualize the interface between the northern down going suduction limb of an Australian thermal convection roller cell and a side-slipping transcurrent portion of a Pacific roller thermal convection cell were unsatisfactory. And, bear in mind that this geometric setting persisted for more than 40 Myr.

In a thermal convecting mantle, phase changes were expected (and observed mineralogically in exposed eroded uplifted arcs). Some proposed e.g. Hager (1981), that the subducted limb depressed the CMB leading to a second negative mass anomaly, which together with that of the negative mass anomaly from the depression of the seafloor at the trench, masked that of the positive mass signal of the dense subducted oceanic crust material. It was not until the single point-mass depth result for the South American Andes site demonstrated only a single point mass depth accounted for that positive Andes anomaly (Bowin, 2000, Fig. 13 SA). This location happens also to lie above a zero contour line in the degree 2–3 field, which indicates no contribution from a density contrast mass anomaly at the core-mantle boundary.

SED
7, 1059–1076, 2015

So, if the mantle of the Earth is not convecting thermally, why is it in motion? When ocean crust is subducted to depths in the upper mantle its minerals of pyroxene and olivine are subjected to increased pressure and converted to higher density phases, and thus create the second greatest mass anomalies in our planet, which produce in the spherical harmonic degree 4–10 field the positive band of positive subduction (10^{22} g). The greatest mass anomalies are restricted to spherical harmonic degrees 2–3 and have magnitudes of 10^{23} g due to irregularities in topography of the Earth's Core-mantle boundary (CMB). Thus, it is only the smaller mass anomalies of the falling dense masses of the phase change mass anomalies that conserve the angular momentum of the global plate tectonic system. The unanswered question now shifts to how does such a planetary system of conservation of angular momentum become activated?

5 Quantifying a deformation index value

Since we can now view "mountain building" deformation as resulting from changes of momentum or impulse, how might such deformations be quantized? Topographic perturbations from a global mean value are a first order measure of a degree of uplift or subsidence that has occurred in a region, but we sought a deformation index value that would be a more relevant than simply a local topographic mean or standard deviation or a combination value. Our selection for this initial test of a deformation index value is to use at each 5 arcmin pixel, the maximum absolute difference with its eight adjacent neighboring pixel. We used this means to estimate the absolute maximum local topographic gradient value at each grid location.

Figure 3 presents our first global view of approximately nine million maximum topographic gradient values at 5 arcmin spacing using a color scale weighted for equal numbers of data values at each color. Here, in addition to the reds associated with the mountainous belts of the Himalayan and Andean ranges, and Island arcs of the world, they also locate the undersea South Atlantic mid-ocean rises. And, in the northwestern

SED
7, 1059–1076, 2015

Pacific Ocean basin, a series of non-red nearly east–west trending, quasi-equally spaced, fracture zone features stand out.

Our next step was to test the extent to which our topographic gradient values might aid in distinguishing deformation magnitudes between areas. For this second test we selected the Himalayan region (Fig. 4) and the western United States (Fig. 5). The same non-weighted color display scale was used to facilitate comparison of their deformation index values. It is clear that significantly higher index values occur in the Himalayan region than in western United States. These local regional results are encouraging, but also prod us to improve our methodology. Further deformation index experiments utilizing multiple parameters and ratios will be tested while awaiting comment on this initial submission.

The Supplement related to this article is available online at doi:10.5194/sed-7-1059-2015-supplement.

Acknowledgements. We wish to thank the following for helping us in solving a variety of problems in developing and maintaining functioning computer hardware and software systems: Christine Hammond, Julie Allen, John Krauspe, Randy Manchester, Eric Cunningham, Tim Barber, Gregory Pike, and Janet Fredericks. Christina Cuellar helped assemble, and format convert tables and illustrations, as well as aiding final manuscript preparation. Bowin thanks the Woods Hole Oceanographic Institution for USD 1500 annual Emeritus research support.

References

Bird, P.: An updated digital model of plate boundaries, Geochem. Geophy. Geosy., 4, 52 pp., 2003.

Bowin, C.: Mass anomaly structure of the Earth, Rev. Geophys., 38, 3, 355–387, 2000.

Bowin, C.: Plate tectonics conserves angular momentum, eEarth, 5, 1–20, doi:10.5194/ee-5-1-2010, 2010.

SED
7, 1059–1076, 2015

Bowin, C. and Kuiper, H.: Resolving accelerations of Earth's Plate tectonics, Poster at AGU Meeting Toronto, Canada, Abstract No. #T43C-01, available at: ftp://ftp.whoi.edu/pub/users/cbowin, 2005.

Constant, J.: Angular Momentum Puzzle Series: Gravitation, Book 17, available at: https://www.smashwords.com/books/view/514937 (last access: February 2015), 2015.

Gripp, A. E. and Gordon, R. G.: Current plate velocities relative to the hotspots incorporating the NUVEL-1 global plate motion model, Geophys. Res. Lett., 17, 1109–1112, 1990.

Hager, B. H.: Subducted slab and the geoid: constrains/ts mantle reology and flow, J. Geophys. Res., 89, 6003–6015, 1984.

Jekeli, C.: Alternative Methods to Smooth the Earth's Gravity Field, Project Report, The Ohio State University, Ohio, 1981.

Pellinen, L. P.: A method for expanding the gravity potential of the Earth in spherical harmonics, Translation ACIC-TC-1282, NTIS: AD-661819, Moscow, 1966.

SED
7, 1059–1076, 2015

Table 1. Euler pole and angular velocity estimates; based on Pacific plate absolute rotation from Morgan and Morgan (2007).

		Relative to PA						Absolute					
		Euler Pole degrees		Angular Velocity degrees per million years				Euler Pole degrees		Angular Velocity degrees per million years			
ID	Plate	Latitude	Longitude	Magnitude	Direction			Latitude	Longitude	Magnitude	Direction		
					X	*Y*	*Z*				*X*	*Y*	*Z*
1	AF	59.160	−73.174	0.927	0.148	−0.491	0.859	43.068	−24.555	0.154	0.664	−0.304	0.683
2	AM	57.645	−83.736	0.931	0.058	−0.532	0.845	47.023	−77.471	0.131	0.148	−0.665	0.732
3	AN	64.315	−83.084	0.870	0.052	−0.430	0.901	69.152	72.937	0.100	0.104	0.340	0.935
4	AP	33.639	−81.177	0.916	0.128	−0.823	0.554	−27.269	−76.653	0.400	0.205	−0.865	−0.458
5	AR	59.658	−33.193	1.162	0.423	−0.277	0.863	33.902	10.771	0.559	0.815	0.155	0.558
6	AS	74.275	−87.237	0.650	0.013	−0.271	0.963	−15.574	96.510	0.243	−0.109	0.957	−0.268
7	AT	56.283	8.932	1.640	0.548	0.086	0.832	33.335	32.439	1.226	0.705	0.448	0.550
8	AU	69.080	1.742	1.074	0.357	0.011	0.934	29.853	50.295	0.629	0.554	0.667	0.498
9	BH	12.559	87.957	0.303	0.035	0.975	0.217	−41.586	91.990	0.941	−0.026	0.748	−0.664
10	BR	45.900	−111.000	0.200	−0.249	−0.650	0.718	−62.004	106.970	0.619	−0.137	0.449	−0.883
11	BS	16.007	122.442	2.125	−0.516	0.811	0.276	−2.480	117.942	2.415	−0.468	0.883	−0.043
12	BU	8.894	−75.511	2.667	0.247	−0.957	0.155	−7.103	−73.760	2.249	0.278	−0.953	−0.124
13	CA	54.313	−79.431	0.904	0.107	−0.573	0.812	19.074	−60.781	0.134	0.461	−0.825	0.327
14	CL	10.130	−45.570	0.309	0.689	−0.703	0.176	−67.700	46.992	0.688	0.259	0.277	−0.925
15	CO	36.823	−108.629	1.998	−0.256	−0.759	0.599	22.317	−116.239	1.334	−0.409	−0.830	0.380
16	CR	−12.628	175.127	3.605	−0.972	0.083	−0.219	−22.274	168.708	3.901	−0.907	0.181	−0.379
17	EA	28.300	66.400	11.400	0.352	0.807	0.474	24.386	67.477	11.418	0.349	0.841	0.413
18	EU	61.066	−85.819	0.859	0.035	−0.483	0.875	82.549	−125.636	0.062	−0.076	−0.105	0.992
19	FT	−10.158	−178.305	4.848	−0.984	−0.029	−0.176	−17.805	176.821	5.054	−0.951	0.053	−0.306
20	GP	9.799	79.690	5.275	0.176	0.970	0.170	2.122	80.790	5.598	0.160	0.986	0.037
21	IN	60.494	−30.403	1.103	0.425	−0.249	0.870	30.740	17.045	0.528	0.822	0.252	0.511
22	JF	35.000	26.000	0.507	0.736	0.359	0.574	−30.453	60.181	0.789	0.429	0.748	−0.507
23	JZ	35.910	70.166	22.520	0.275	0.762	0.587	33.923	70.693	22.430	0.274	0.783	0.558
24	KE	47.521	−3.115	2.831	0.674	−0.037	0.738	36.355	9.218	2.357	0.795	0.129	0.593
25	MA	43.777	149.205	1.278	−0.620	0.370	0.692	9.106	133.230	1.224	−0.676	0.719	0.158
26	MN	−3.037	150.456	51.300	−0.869	0.492	−0.053	−3.789	150.080	51.573	−0.865	0.498	−0.066
27	MO	59.589	78.880	0.893	0.098	0.497	0.862	5.316	86.493	0.857	0.061	0.994	0.093
28	MS	11.103	−56.746	4.070	0.538	−0.821	0.193	1.468	−53.682	3.640	0.592	−0.805	0.026
29	NA	48.709	−78.167	0.749	0.135	−0.646	0.751	−51.875	−48.699	0.163	0.407	−0.464	−0.787
30	NB	−4.000	139.000	0.330	−0.753	0.654	−0.070	−46.155	114.429	0.989	−0.286	0.631	−0.721
31	ND	58.664	−89.003	0.701	0.009	−0.520	0.854	−60.423	123.324	0.106	−0.271	0.412	−0.870
32	NH	13.000	−12.000	2.700	0.953	−0.203	0.225	−1.873	−3.134	2.543	0.998	−0.055	−0.033
33	NI	6.868	−168.868	3.255	−0.974	−0.192	0.120	−5.356	−176.147	3.227	−0.993	−0.067	−0.093
34	NZ	55.578	−90.096	1.360	−0.001	−0.565	0.825	49.949	−95.741	0.563	−0.064	−0.640	0.765
35	OK	55.421	−82.859	0.845	0.071	−0.563	0.823	4.138	−70.042	0.072	0.340	−0.937	0.072

SED
7, 1059–1076, 2015

Table 1. Continued.

		Relative to PA						Absolute					
		Euler Pole degrees		Angular Velocity degrees per million years				Euler Pole degrees		Angular Velocity degrees per million years			
ID	Plate	Latitude	Longitude	Magnitude	Direction X	Direction Y	Direction Z	Latitude	Longitude	Magnitude	Direction X	Direction Y	Direction Z
36	ON	48.351	142.415	2.853	−0.527	0.405	0.747	33.309	134.502	2.625	−0.586	0.596	0.549
37	PA	0.000	0.000	0.000	1.000	0.000	0.000	−59.330	94.900	0.803	−0.044	0.508	−0.860
38	PM	54.058	−90.347	0.907	−0.004	−0.587	0.810	18.588	−107.084	0.137	−0.278	−0.906	0.319
39	PS	−1.200	−45.800	1.000	0.697	−0.717	−0.021	−44.243	−25.003	1.020	0.649	−0.303	−0.698
40	RI	36.700	−105.200	4.692	−0.210	−0.774	0.598	32.016	−107.586	3.987	−0.256	−0.808	0.530
41	SA	54.999	−85.752	0.636	0.042	−0.572	0.819	−75.217	100.241	0.175	−0.045	0.251	−0.967
42	SB	10.610	−32.990	8.440	0.824	−0.535	0.184	6.122	−30.689	8.097	0.855	−0.507	0.107
43	SC	48.625	−81.454	0.652	0.098	−0.654	0.750	−80.395	−31.677	0.204	0.142	−0.088	−0.986
44	SL	63.121	−97.084	0.856	−0.056	−0.449	0.892	40.224	163.787	0.113	−0.733	0.213	0.646
45	SO	58.789	−81.637	0.978	0.075	−0.513	0.855	55.293	−67.498	0.178	0.218	−0.526	0.822
46	SS	19.529	135.017	1.478	−0.667	0.666	0.334	−6.491	126.226	1.738	−0.587	0.802	−0.113
47	SU	55.447	−72.955	1.103	0.166	−0.542	0.824	42.103	−52.024	0.325	0.457	−0.585	0.670
48	SW	−19.019	−39.640	1.840	0.728	−0.603	−0.326	−41.053	−28.277	1.964	0.664	−0.357	−0.657
49	TI	19.524	112.175	1.514	−0.356	0.873	0.334	−5.783	108.348	1.831	−0.313	0.944	−0.101
50	TO	28.807	2.263	9.300	0.876	0.035	0.482	24.970	5.143	8.980	0.903	0.081	0.422
51	WL	22.134	132.330	1.546	−0.624	0.685	0.377	−3.483	124.268	1.778	−0.562	0.825	−0.061
52	YA	69.067	−97.718	0.998	−0.048	−0.354	0.934	67.697	146.639	0.261	−0.317	0.209	0.925

SED
7, 1059–1076, 2015

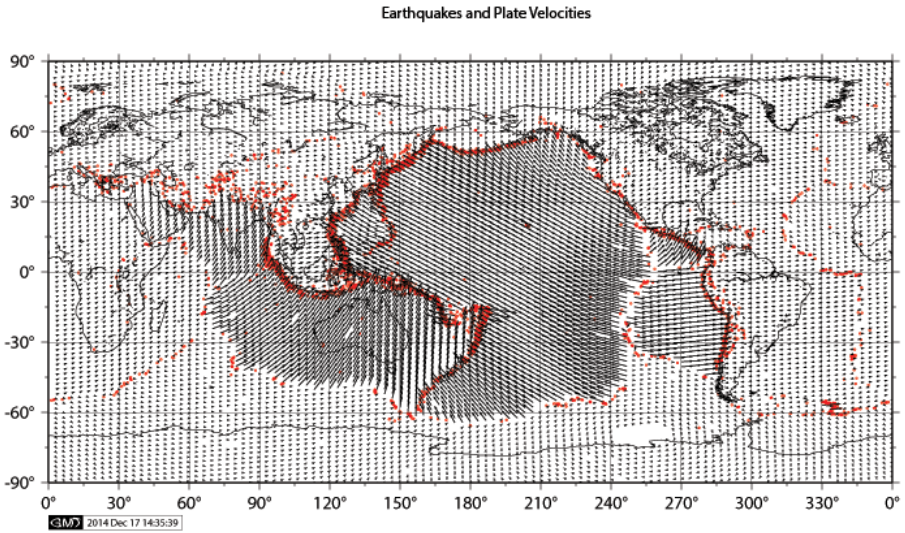

Figure 1. Absolute plate velocity vectors (1 per 1000 plotted black arrows) for the 52 plates of Bird (2003) and earthquake locations with magnitudes greater than magnitude 6.0.

SED
7, 1059–1076, 2015

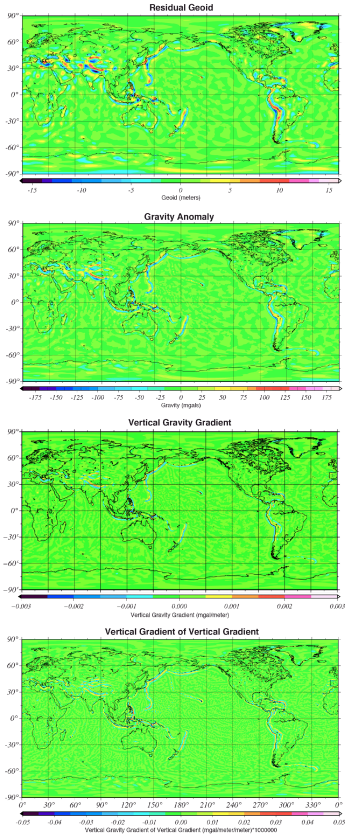

Figure 2. Residual geoid, gravity, vertical gravity gradient, and vertical gradient of vertical gravity gradient for spherical harmonic degrees 31–464. Color scale weighted so that each color has the same number of data samples.

SED
7, 1059–1076, 2015

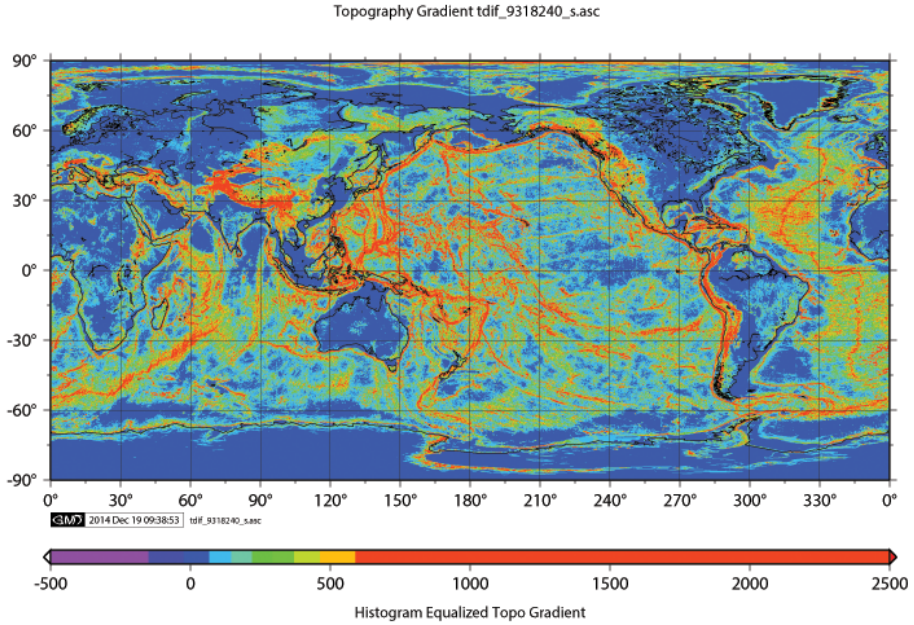

Figure 3. World view of maximum topographic gradient of each 5 arcmin grid point with adjacent 5 arcmin topographic values for the Earth.

SED
7, 1059–1076, 2015

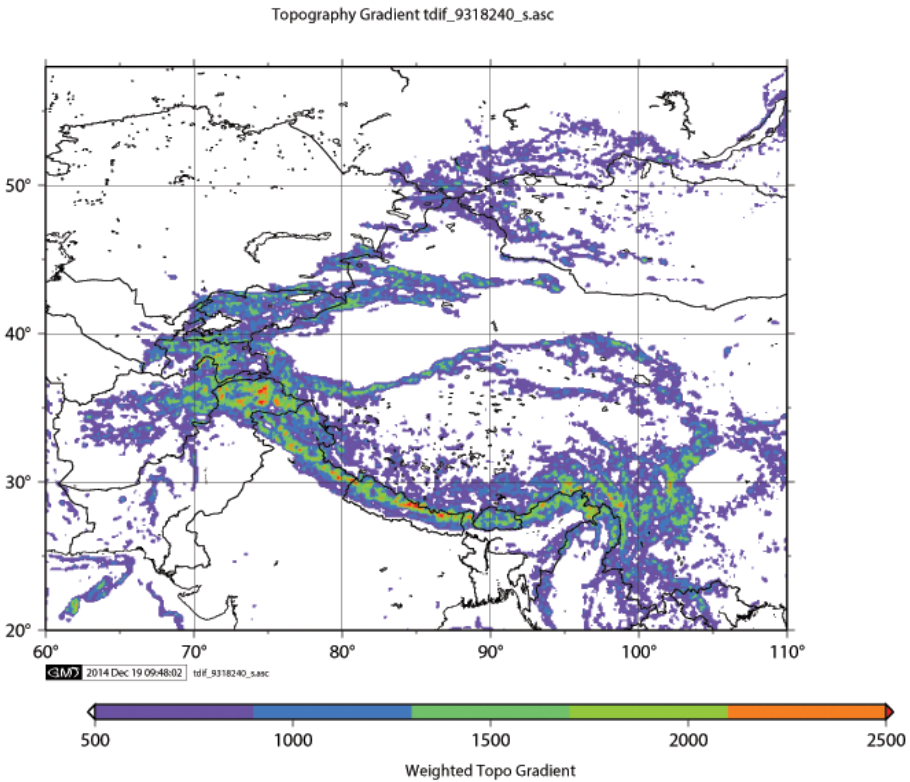

Figure 4. Maximum topographic gradient of each 5 arcmin grid point with its adjacent 5 arcmin values in the Himalayan region. Scale values are not weighted.

SED
7, 1059–1076, 2015

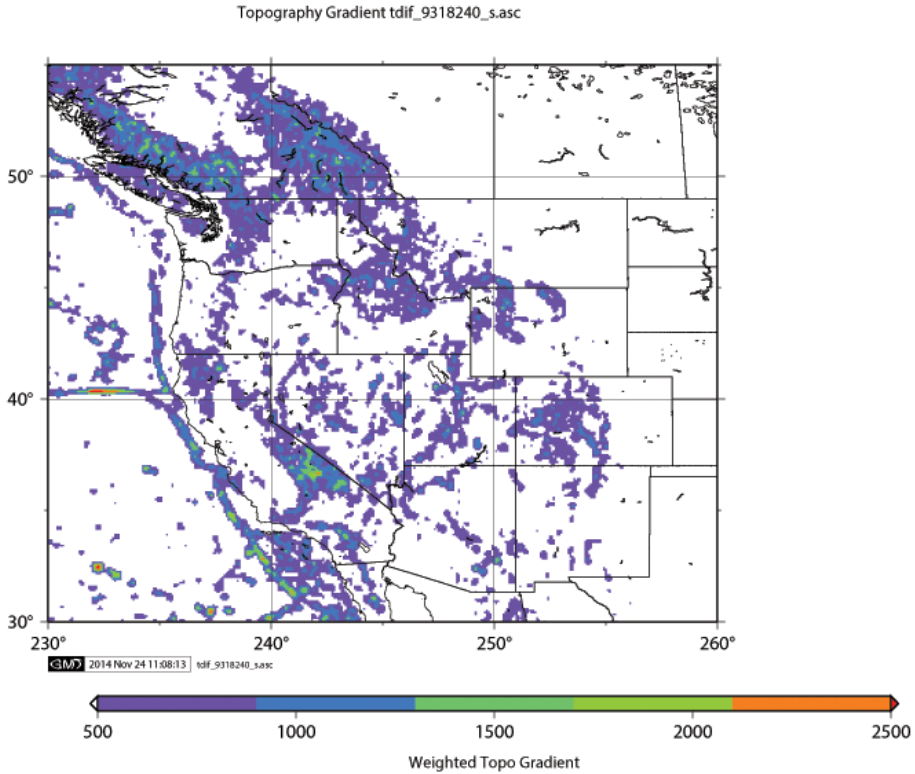

Figure 5. Maximum topographic gradient of each 5 arcmin grid point with its adjacent 5 arcmin values in the western United Sates region. Scale values are not weighted.

SED
7, 1059–1076, 2015